Observing the timescales of aerosol-cloud interactions in snapshot satellite images

Edward Gryspeerdt[1], Tom Goren[2], and Tristan W. P. Smith[3]

[1]Space and Atmospheric Physics Group, Imperial College London, UK
[2]Institute for Meteorology, Universität Leipzig, Germany
[3]UCL Energy Institute, University College London, UK

Correspondence: Edward Gryspeerdt (e.gryspeerdt@imperial.ac.uk)

Abstract. The response of cloud processes to an aerosol perturbation is one of the largest uncertainties in the anthropogenic forcing of the climate. It occurs at a variety of timescales, from the near-instantaneous Twomey effect, to the longer timescales required for cloud adjustments. Understanding the temporal evolution of cloud properties following an aerosol perturbation is necessary to interpret the results of so-called "natural experiments" from a known aerosol source, such as a ship or industrial site. This work uses reanalysis windfields and ship emission information matched to observations of shiptracks to measure the timescales of cloud responses to aerosol in instantaneous (or"snapshot") images taken by polar-orbiting satellites.

As in previous studies, the local meteorological environment is shown to have a strong impact on the occurrence and properties of shiptracks, but there is a strong time dependence in their properties. The largest droplet number concentration (N_d) responses are found within three hours of emission, while cloud adjustments continue to evolve over periods of ten hours or more. Cloud fraction is increased within the early life of shiptracks, with the formation of shiptracks in otherwise clear skies indicating that around 5-10% of clear-sky cases in this region may be aerosol-limited.

The liquid water path (LWP) enhancement and the N_d-LWP sensitivity are also time dependent and strong functions of the background cloud and meteorological state. The near-instant response of the LWP within shiptracks may be evidence of a bias in estimates of the LWP response to aerosol derived from natural experiments. These results highlight the importance of temporal development and the background cloud field for quantifying the aerosol impact on clouds, even in situations where the aerosol perturbation is clear.

1 Introduction

The response of a cloud to an aerosol perturbation is fundamentally time-sensitive. Increasing the number of cloud condensation nuclei (CCN) increases the number of cloud droplets at cloud base (Twomey, 1974) almost immediately, resulting in a near-instantaneous change to the properties of an individual air parcel. The N_d and effective radius (r_e) in the rest of the cloud respond on a timescale related to the cloud geometrical depth and the in-cloud updraught (on the order of 10-20 minutes for a cloud thickness of 200m and an updraught of $0.2\,\mathrm{ms}^{-1}$). This response is referred to as the Twomey effect, which leads to the radiative forcing from aerosol-cloud interactions (RFaci; Boucher et al., 2013).

Changes in droplet size can also impact precipitation processes, leading to further changes in liquid cloud properties, notably the liquid water path (LWP) and cloud fraction (CF; e.g. Albrecht, 1989). Further changes to the LWP and CF may come through aerosol-dependent entrainment and mixing processes (Ackerman et al., 2004; Xue and Feingold, 2006; Bretherton et al., 2007; Seifert et al., 2015). The timescale for these processes is longer than the N_d timescale, as they proceed through a modification of process rates, requiring several hours to generate a significant change in the LWP (Glassmeier et al., 2021). For a large-scale change in cloud amount, the timescales may be even longer, as it requires the switching of cloud regime, from open to closed celled convection (Rosenfeld et al., 2006; Goren and Rosenfeld, 2012). The timescale for this aerosol response is related to the timescale for a switch between open and closed cells and related to the lifetime of individual cells (around 2 hours Wang and Feingold, 2009a).

One of the largest uncertainties when using observations to constrain aerosol-cloud interactions is the impact of meteorological covariations, where aerosol and cloud properties are both correlated to the same meteorological factors (such as relative humidity). Variations in this factor will then generate relationships between aerosol and cloud properties, even without a causal impact of aerosol on cloud (e.g. Quaas et al., 2010). Although a number of methods for identifying causal relationships have been proposed (e.g. Koren et al., 2010; Gryspeerdt et al., 2016; McCoy et al., 2020), "natural experiments" (Rosenzweig and Wolpin, 2000), where the aerosol is perturbed independently of meteorology (such as by ships or industry Conover, 1966; Toll et al., 2019) are the standard way of isolating the causal aerosol effect. As these studies are often performed at relatively short times after the aerosol perturbation, understanding the timescales of the response is essential to interpret these results.

The majority of satellite observations provide a static picture of the Earth, limiting their ability to characterise liquid cloud temporal development. Previous studies have addressed this by using multiple observations to build a composite diurnal cycle. Matsui et al. (2006) showed that the MODIS diurnal cycle is correlated to the aerosol environment, with a clear importance of the initial cloud state. Meskhidze et al. (2009) and Gryspeerdt et al. (2014) showed that short term development is also correlated to the aerosol environment, recently been extended to longer timescales (Christensen et al., 2020).

These studies have focused on existing variability in aerosol. This allows cloud temporal development to be investigated at a global scale, but limits the ability to measure timescales directly. Exogeneous aerosol perturbations (such as those from ships) are emitted independently of meteorological factors. With a limited spatial extent, they have clearly identifiable polluted and control regions, allowing the impact of the aerosol on the cloud field to be inferred (Durkee et al., 2000a), vary along their length (Kabatas et al., 2013) and can be tracked over several days, providing evidence of a long-lasting aerosol perturbation to cloud properties (Goren and Rosenfeld, 2012).

In this work, the temporal development of shiptracks is used to quantify the timescales of aerosol-cloud interactions in marine boundary layer clouds and how these are affected by meteorology. Although shiptracks appear in satellite images as linear cloud formations, they have no ability to transmit information along their length. This means that they can be considered as a chain of independently perturbed clouds with a similar initial aerosol perturbation (Kabatas et al., 2013). By linking shiptracks identified in satellite images (e.g. Segrin et al., 2007) with ship SO_x emissions estimated from transponder data (Smith et al., 2015; Gryspeerdt et al., 2019b), the aerosol perturbation is identified independently of the cloud properties. The ship motion and reanalysis windfield are used to estimate the emitted aerosol trajectory, enabling the conditions controlling

shiptrack formation to be identified and providing a time-axis for the perturbation. This work uses this snapshot method for measuring time dependence of shiptrack macrophysical (length, detectability and width) and microphysical properties (N_d, LWP), their sensitivity to local meteorology and aerosol perturbation, and what this means for the potential radiative forcing.

2 Methods

2.1 Shiptrack locations

This work uses the shiptrack and ship locations from Gryspeerdt et al. (2019b). The shiptracks were logged by hand in MODIS Aqua day microphysics images (Lensky and Rosenfeld, 2008), with the N_d (following Quaas et al., 2006) used in ambiguous cases. These shiptracks are linked to individual ships using ship AIS transponder locations, with emissions estimated using this AIS information and the ship physical properties (Smith et al., 2015). All of the tracks used are linked to ships from 2015 in a region off the coast of California (30-45N, 115-130W).

For each ship, the estimated trajectory of the emitted SO_x is determined by advecting the historical ship positions with the 1000 hPa reanalysis windfield from ERA5 (as in Gryspeerdt et al., 2019b). This level was selected as it provided the best match between the trajectories and the observed shiptrack locations, likely due to the thin boundary layers in this region. For the observed shiptrack, the time since emission is then determined as the time since emission at the closest point on the emission trajectory. This emission trajectory is also used to extend the observed shiptrack to 20 hours since emission.

Ship location data has to be interpolated between sparse AIS observations, which can lead to significant error in the locations. A comparison with ship meteorological reports suggests that this interpolation error can often be as large as 100 km in the ship position, compounding further in the estimated emission trajectories. To avoid this interpolation uncertainty, only cases where normalised Fréchet distance (the maximum distance between points on the two trajectories when they are traversed to minimise this distance) between the reconstructed plume and the identified shiptrack less than 0.5 are included to ensure an unambiguous match between the ship and shiptrack (following Gryspeerdt et al., 2019b). This leaves 1,209 shiptracks for use in this study.

2.2 Identifying polluted regions

The identification of polluted regions is based on the method from Segrin et al. (2007) and Christensen et al. (2009), with modifications outlined in Gryspeerdt et al. (2019b). The identified track is divided into 10 pixel long chunks (each MODIS pixel is 1 km across at nadir, rising to over three at the swath edge). Within each chunk, pixels are classed as "detected" when the N_d is more than 2 standard deviations above the background (excluding the detected pixels). The detected pixels are grouped with nearby pixels; groups that do not intersect hand-identified track central location or location from the previous segment are classed as "polluted (non-track)" and excluded from this analysis. Fig. 1a shows an example, with the detected shiptrack in the centre and a second shiptrack at the edge that has been excluded due to being too far from the hand-identified shiptrack location. The edges of the shiptrack within each chunk are defined by the furthest spaced detected pixels, with extra pixels in that region being classed as "polluted". This polluted regions is used to compile the statistics in this work.
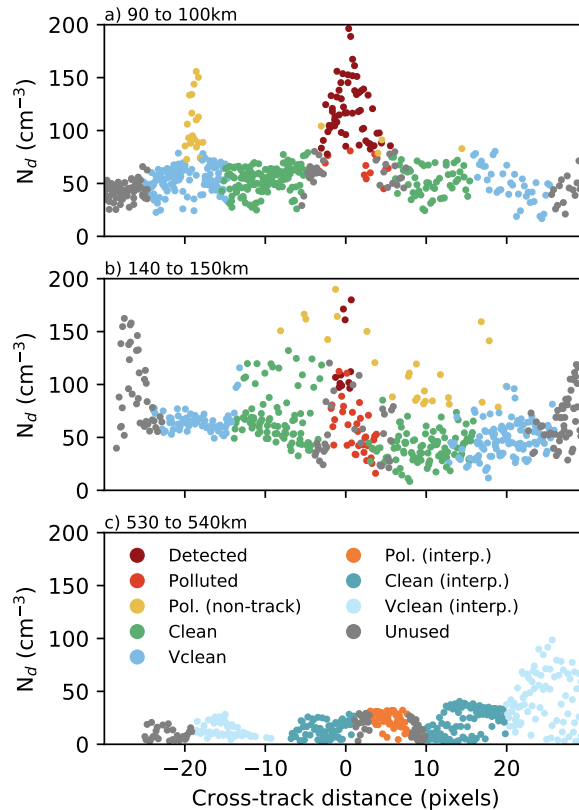
Figure 1. Example track chunks and the identification of polluted pixels along the track shown in Fig. 2. Marker colours are shown in (c). Distances in the titles are from the ship location at the time of the satellite overpass. "Detected" pixels are those located by the Segrin et al. (2007) algorithm. "Polluted" pixels are added to the in-shiptrack region by the modifications in this work. "Polluted (non-track)" pixels were detected, but removed from the shiptrack region in this work. The "clean" pixels are used as an unperturbed control situation, while "vclean" is a further control. The interpolated pixels (c) are from segments where no detected pixels exist. Further details are in the text.

With a buffer region of two pixels ($>2\,\text{km}$), corresponding clean/control regions are identified 10 pixels either side of the track and "vclean" regions a further 10 pixels either side of that. Distances are in pixels to keep an approximately similar number of pixels in each region for each segment. The clean and vclean regions exclude the polluted (non-track) pixels, as nearby shiptracks (as shown in Fig. 1a) are not representative of the background cloud state. This may not always be the

5 correct decision, as crossing shiptracks (Fig. 1b) may be more representative of the background, but it has little impact on the results presented in this work.

The classifications are then aggregated into 15 minute (10 km) segments. This is a short enough time period to allow the initial development of the track to be resolved and these two measures are approximately equal for relative windspeed of $40\,\text{kmh}^{-1}$ (Durkee et al., 2000a). A full 20 hour shiptrack classification is shown in Fig. 2b, with the flag colours following

10 Fig. 1. Only 20,175 segments (out of 96,720 total) contain detected pixels. To identify polluted pixels in segments where there
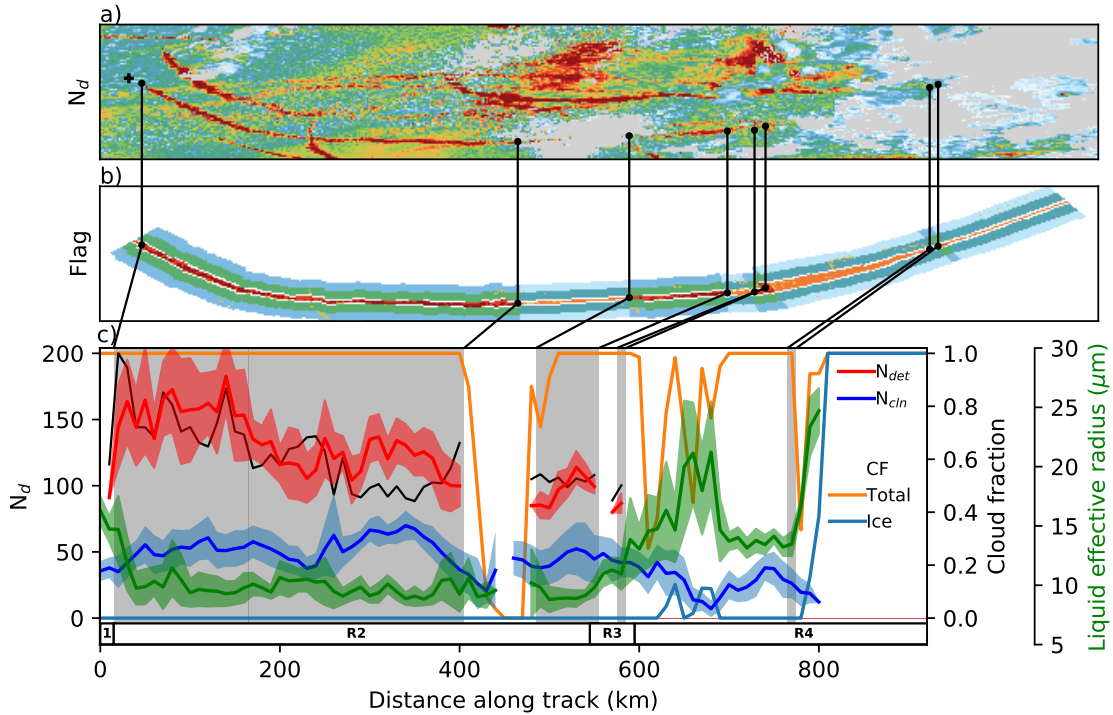
Figure 2. An example shiptrack. a) The N_d field from MODIS, grey regions indicate no liquid cloud. The ship position is marked with a cross and the dot markers are to identify regions of the shiptrack. b) Pixels as identified by the shiptrack algorithm. Red regions are polluted regions of the shiptrack and green the corresponding clean regions. Orange regions are interpolated shiptrack locations, based on the identified polluted regions as described in the text. Blue regions are the corresponding unperturbed regions for the interpolated shiptrack locations. c) The change in properties along the shiptrack. Grey regions are "detected" shiptrack segments (polluted pixels are identified) and the black lines connect the edges of these regions between subplots. The R2 region along the bottom shows the section of the track identified by a human from the day-microphysics imagery. Note that these do not have to overlap. Red is N_{pol} for regions where the shiptrack is detected and blue N_{cln} with the shaded regions showing the standard deviation within that segment. The thin black line is the N_d enhancement, ε_N (N_{pol}/N_{cln}). The unperturbed r_e and standard deviation are shown in green. The total CF is in orange and the ice CF in light blue.

are no detected pixels, the width from the nearest segment with a detected pixel is interpolated along the estimated emissions trajectory (even within the hand-identified region (R2 in Fig. 2c).

Cloud properties are recorded along the length of the shiptrack, for both polluted pixels and the corresponding clean/control region outside the track (Fig. 2c). The N_d, for polluted (red; N_{pol}) and unperturbed (blue; N_{cln}) regions, is calculated following the method of Quaas et al. (2006), applying the filtering as outlined in Grosvenor et al. (2018). In this example, there is a general decrease in N_d along the length of the shiptrack, but with a considerable fluctuation. The detected N_d enhancement factor (thin black line; $\varepsilon_N = N_{pol}/N_{cln}$) shows a much smoother decrease, as it incorporates correlated fluctuations in N_{pol} and N_{cln}.

The retrieved cloud properties in this work are from the MODIS Aqua collection 6.1 cloud product (MYD06L2; Platnick et al., 2017) and the meteorological properties are from the ERA5 reanalysis. Supplemental information about the background aerosol comes from the sulphate concentration in the MERRA reanalysis, following McCoy et al. (2017).

The uncertainties throughout this work are calculated using a bootstrap method (Efron, 1979) with 1000 samples and are shown with a 16-84% uncertainty range. This range is chosen such that significance at an individual time between high and low SO_x is indicated by the non-overlap of these ranges.

2.3 Potential radiative forcing

To compare the radiative effect of shiptracks in different conditions, a potential radiative forcing (PRF) is calculated following Eq.1. This is not the true radiative forcing of the shiptrack, as it ignores diurnal variations in the cloud response to aerosol and incoming solar flux ($F^\downarrow$; approximated by a constant $280\,\mathrm{Wm}^{-2}$).

$$PRF = F^\downarrow A \left((\alpha_{pol} - \alpha_{surf}) CF_{pol} - (\alpha_{cln} - \alpha_{surf}) CF_{cln} \right) \tag{1}$$

The PRF is calculated for each segment individually, with A denoting the area of the polluted region within the segment. The cloud albedo (α) is calculated from the cloud optical depth (τ) following Eq. 2 (Bohren, 1987). The surface ocean albedo is taken as a constant 0.04 (a representative value from Jin et al., 2004). Only liquid clouds are considered in the CF (derived from "Cloud_Phase_Optical_Properties"). The impact of CF changes is calculated by setting $CF_{pol} = CF_{cln}$ to exclude the impact of CF adjustments.

$$\alpha = \frac{\tau}{\tau + 13.3} \tag{2}$$

3 Results

The results from this work are split into two sections, the first deals with the macrophysical properties of the shiptrack (length, width, detectability, CF), whereas the second focuses on the microphysical properties and the liquid water path.

3.1 Macrophysical properties

3.1.1 Track length

The median shiptrack in this study is last observed at a distance of about $200\,\mathrm{km}$ from the source ship, with longer shiptracks more commonly observed behind ships with higher SO_x emissions (Fig. 3a). The difference is significantly reduced when using time as a coordinate (Fig. 3b), due to faster ships (producing longer shiptracks) typically burning more fuel and so emitting more SO_x. To account for this, we use time since emission as the along-track coordinate throughout the rest of this work.
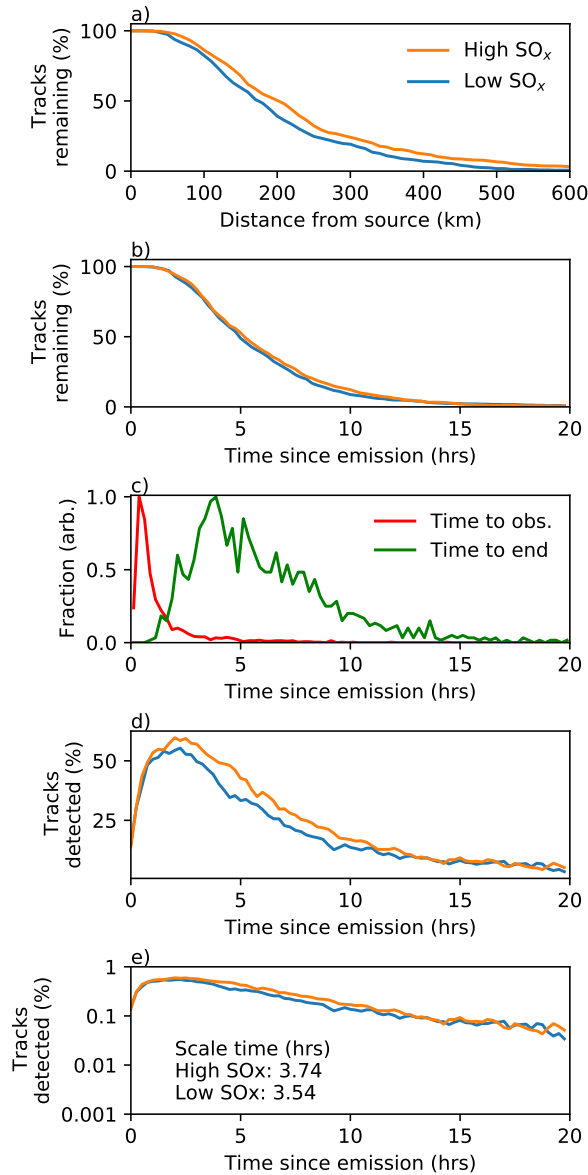
Figure 3. a) Track length (distance to oldest observed segment) for ships with high and low SO$_x$ emissions. b) The same as (a), but using the time since emission instead of the distance. c) Histograms showing the time to first observation (red) and last observation (green) for the tracks used in this study. d) The percentage of tracks that are "detected" within any given 15 minute segment. Note that this is less than 100% in many cases due to gaps in shiptracks. e) as (d) but with a log y-axis.

There is a large variation in the time to initial observation (time to obs.) and the time to last observation for the shiptracks in this work (Fig. 3c). As in previous studies (Durkee et al., 2000b), the mean time to a first observation of the shiptrack is under

an hour, with this database having a mean of 45 min. There is a long tail, with some tracks not being observed until five hours since emission. These long times before initial observation are due to a lack of cloud at ship locations and the identification of time from distance, rather than decoupling increasing the time to cloud (Liu et al., 2000). A large variation in the length of the observed section of the shiptrack is also found, with a median length of five hours but some lasting only an hour and others

5 lasting almost 20. The tracks in this work are on average shorter than those in Durkee et al. (2000a) and Schreier et al. (2007), partially due to differences in the criteria used to select the tracks.

Many of these shiptracks have gaps (segments where the track is not detected). The maximum detected fraction is around 1-2 hours after emission, where each 15 min segment has an approximately 60% chance of containing a detected shiptrack (Fig. 3d). Although the difference is small, ships with higher SO_x emissions produce shiptracks that are more likely to be detected for

10 a longer period of time (Fig. 3d, e). This suggests that also the overall lifetime for the whole population of shiptracks is not a strong function of SO_x, ships with larger SO_x emissions are more likely to generate tracks that can be detected for a longer period of time and so might be expected to have a larger radiative impact.

3.1.2 Track detection/formation
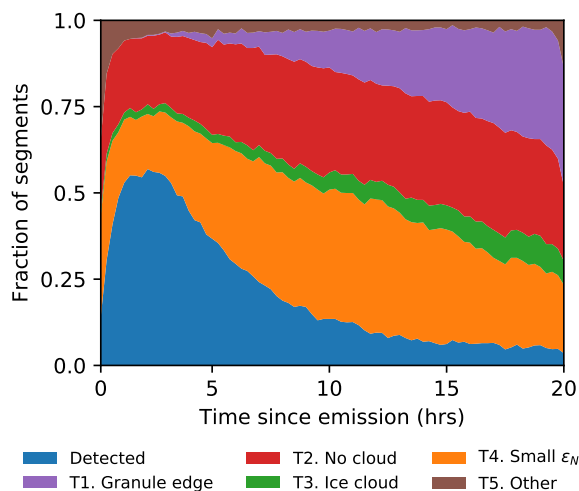
Figure 4. Reasons for track non-detection in segments as a function of time since emission. The tests are applied in the order T1-4.

The majority of segments do not contain a detected track; what limits shiptrack formation in these segments? For each

15 segment lacking a detected track, four tests are applied in order: T1, is the segment outside a MODIS image (granule); T2, is there no cloud in the segment; T3, is the segment ice cloud and T4, is the ε_N less than 1.4 (a 40% enhancement)? The percentage of segments satisfying these tests are shown in Fig. 4, with the tests being applied in order (so segments with satisfying T2 are not checked for T3 or T4).

Although many shiptracks are located close to the edge of a MODIS image ("granule"), only a small number of shiptracks disappear because they reach the edge of the MODIS granule. Around 30% of shiptracks reach a granule edge after 20 hours after emission. In around 25% of segments, a lack of cloud prevents the detection of a shiptrack. This is expected given the CF in this region and is approximately constant with time since emission. Similarly, the small impact of overlying ice cloud on the detection of shiptracks is primarily due to the low ice CF in subtropical subsidence regions.

The impact of a small ε_N increases with time since emission. Without the individual history of the segments, it is not possible to conclusively separate the dissipation of the shiptrack from an increased background N_d. The small ε_N (T4) provides an indication of segments which could potentially form detectable shiptracks with increases in ship SO_x emissions, although meteorological conditions will also prevent the formation or observation of shiptracks in some conditions (Noone et al., 2000; Possner et al., 2018; Gryspeerdt et al., 2019b). Even in a region with large amounts of low-level liquid cloud, the frequency of occurrence of liquid cloud is a significant control on the length of shiptracks.

3.1.3 Track widths
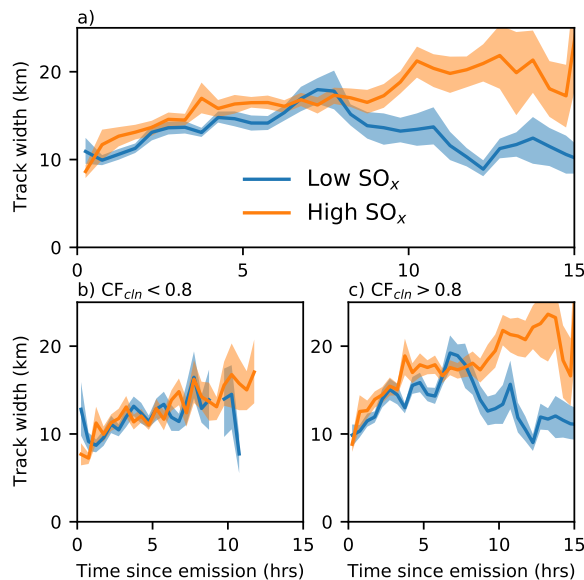
Figure 5. a) Shiptrack width as a function of time since emission for high (orange) and low (blue) SO_x emitting ships. b) as (a) but only for segments with a CF_{cln} <0.8, c) as (a) for segments with a CF_{cln} >0.8. Averaged over half hour periods.

Shiptrack width (defined as the maximum cross-track distance between polluted pixels within a segment) increases gradually with time since emission (Fig. 5a), similar to previous studies (Durkee et al., 2000a). Although the shiptrack width is highly sensitive to outlier polluted pixels, a weak dependence of width on SO_x emissions is observed, with a larger width for higher SO_x emissions.

This sensitivity of track width to SO_x depends on the background cloud state. Considering only segments with a lower out-of-track CF ($CF_{cln}<0.8$), the width rises slowly over time, but with little sensitivity to the initial aerosol perturbation (Fig. 5b). In contrast, the high CF_{cln} segments have a width that is more sensitive to the ship SO_x emissions (Fig. 5c).

Differences in the cloud regimes indicated by CF_{cln} may explain this difference in behaviour. Lower CF_{cln} situations are more likely to be open celled stratocumulus (Muhlbauer et al., 2014). In this situation, the width of the track is controlled primarily by the cell width, rather than the aerosol perturbation, due to a less efficient mixing of aerosol between cells (Scorer, 1987). Over time, mixing between the cells due to the collapse and creation of new open cells (Feingold et al., 2010) allows the track to widen, gradually affecting a wider region as more cells are included in the track.

The high CF_{cln} situation is more likely to be closed-celled stratocumulus or sea-fog (Ackerman et al., 1993). Particularly in the sea-fog case, the lack of a strong cellular structure control on the shiptrack width allows a dependence on the SO_x emissions, with higher SO_x emissions creating a wider plume and so a wider initial shiptrack. The quick and continued growth of the shiptrack in the first five hours for these high CF_{cln} cases (Fig. 5c) therefore may be linked to this initial plume dispersion. Similar to the low CF_{cln} case, the gradual growth in the plume over time after this fast-growth period may be linked to cloud processes and mixing. Future model studies will be useful to identify the factors controlling the growth of the shiptrack width.

3.1.4 Controls on track length

Given the strong impact of cloud occurrence on the disappearence of shiptracks (Fig. 4), factors controlling liquid cloud occurrence will also have an effect on the shiptrack length. The estimated inversion stability (EIS; Wood and Bretherton, 2006) has a strong link to low cloud cover in this region, but a comparison between high and low EIS environments shows only a 20% increase in the median lifetime, from five to six hours (Fig. 6a). This weak effect is primarily due to the prevalence of short shiptracks in this work and the time-dependent impact of meteorology on shiptrack lifetime.

Normalising by the total number of shiptracks remaining in the total sample highlights a much clearer role for meteorology, with shiptracks in low average EIS environments only half as likely to have a lifetime longer than ten hours compared those with in a higher EIS environment, due to the lower cloud fraction (Fig. 6b). The low cloud fraction also impacts the sensitivity to SO_x emissions, with the lifetime of shiptracks in low EIS environments being almost insensitive to SO_x emissions. In contrast, the lifetime of high EIS shiptracks is much more sensitive to SO_x emissions, as the high CF makes dissipation processes more important. This is supported by studies aiming to produce a climatology of shiptracks finding more shiptracks in regions of extensive low cloud cover (Schreier et al., 2007).

Despite a strong controlling influence on the formation of shiptracks (Gryspeerdt et al., 2019b), cloud top humidity has a much weaker impact on shiptrack length. Drier cloud tops typically indicate longer shiptracks, perhaps due to an increased in-cloud updraught and so higher sensitivity to aerosol (Lilly, 1968). A slight decrease in shiptrack length is observed for moister cloud tops.

Windspeed has a stronger influence on shiptrack length, with higher windspeeds producing shorter shiptracks. Although shiptrack formation is more common at high windspeeds (Gryspeerdt et al., 2019b), these shiptracks are typically shorter and have a length that is initially less sensitive to the size of the aerosol perturbation. This may be due to a number of factors. Sea
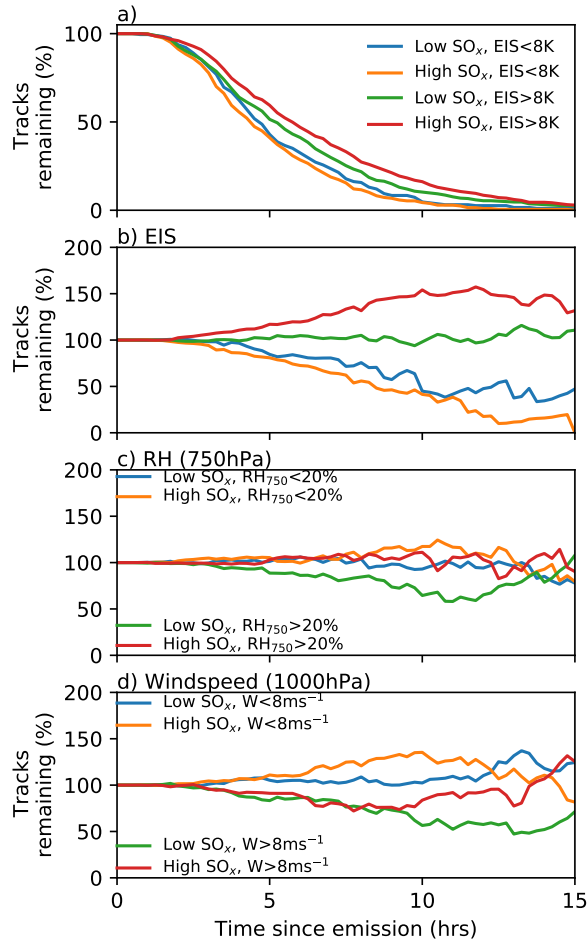
Figure 6. Shiptrack length as function of meteorological parameters. a) The percentage of tracks remaining for high and low SO_x emissions for high and low EIS (averaged along the track). b) The percentage of tracks remaining as a fraction of the fraction of tracks remaining in the total dataset, comparing the impact of emissions at high and low EIS. c) As (b) but for cloud top relative humidity (750hPa). d) As (b) but for high and low 1000 hPa windspeed.

salt production is enhanced at high windspeeds, which may lead to a decrease in N_d, perhaps through giant CCN production (Lehahn et al., 2011; Gryspeerdt et al., 2016; McCoy et al., 2017), an increase in precipitation and so a reduction in the impact of the aerosol perturbation.

3.1.5 Cloud fraction enhancement

As well as creating increases in N_d that allow their detection, the shiptracks in this study also have a higher cloud fraction than the control region (Fig. 7). An average increase of around 3% over the first ten hours is observed, peaking around 3-4 hours after
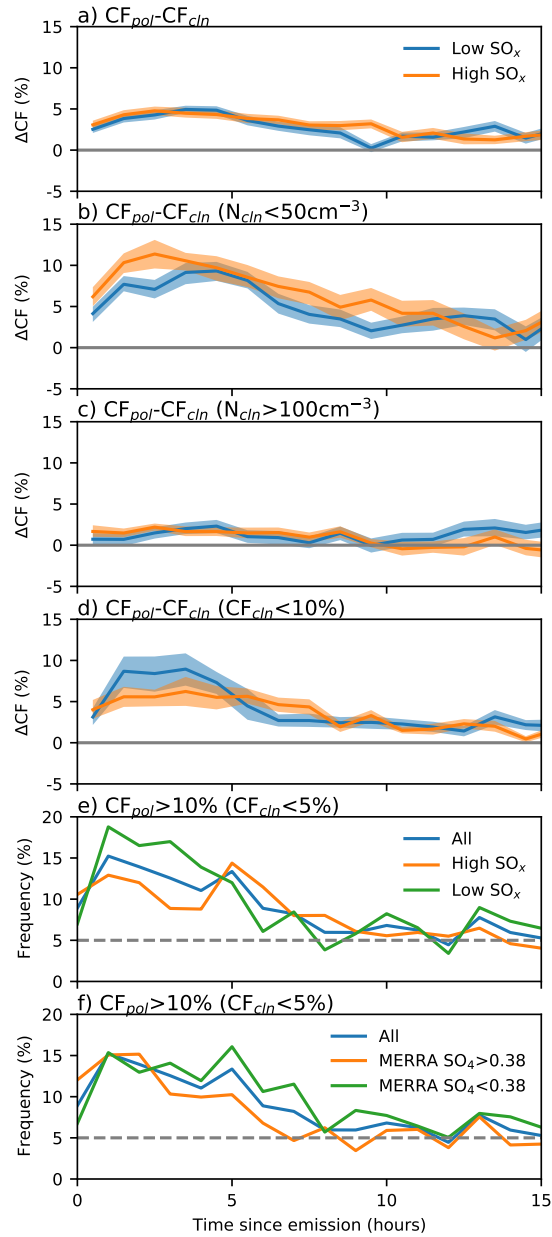
Figure 7. a) Cloud fraction in the polluted shiptrack regions compared to the corresponding clean locations. b) as (a) but only for cases where the N_d in the clean region is $<50 \text{cm}^{-3}$. c) as (a) but only for cases where the N_d in the clean region is $>100 \text{cm}^{-3}$. d) as (a) but only for cases where the CF_{cln} is $<10\%$. e) the percentage of cases with $CF_{pol}>10\%$ and $CF_{cln}<5\%$, stratified by the ship SO_x emissions. f) as (e) but stratified by reanalysis/background SO_4. Grey lines are gridlines.

emission. The CF increase is not strongly correlated to the ship SO_x emissions (Fig. 7a), but varies significantly as a function of the background cloud state. In relatively clean conditions (N_{cln} <50cm^{-3}), the CF is increased by almost 10% within the first five hours after emission (Fig. 7b). In contrast, the CF in already polluted conditions does not increase significantly inside the shiptrack (Fig. 7c), partly due to the higher CF found at higher N_d (e.g. Gryspeerdt et al., 2016) restricting the opportunity for any further CF increase within the shiptrack.

By estimating the ship aerosol trajectories, shiptrack are located even when there are no surrounding clouds (preventing the detection algorithm from operating). By selecting cases with a low CF_{cln} (<10%), a 3-7% increase in cloud amount (ΔCF) is found in the early stages of the shiptrack (Fig. 7d). The ΔCF is concentrated in a small fraction of segments; in the first 5 hours of the shiptrack, of the segments with a $CF_{cln} < 5\%$ only 10% have a $CF_{pol} > 10\%$ (Fig. 7e). A CF increase is more common in cases with lower SO_x increases, but does not appear to be correlated to the reanalysis background aerosol (Fig. 7f). These segments with a low CF_{cln} but higher CF_{pol} (Fig. 7e) are potential aerosol-limited CF cases.

By selecting cases with a low CF_{cln}, random biases in the CF will increase ΔCF (as CF cannot be less than 0%). This gives the appearance of an aerosol-limited CF, increasing the fraction of potentially aerosol-limited cases. As this effect is independent of time since emission, the asymptote to 5% of potential aerosol limited cases (>10 hours in Fig. 7) provides a simple estimate of this bias. Although this would suggest that up to 5% of the potentially aerosol-limited cases in the early stages of the shiptrack development are the result of this bias, it leaves around 5% of clear-sky cases as aerosol-limited (Fig. 7e). However, as this estimate relies on gaps in and dissipation of existing shiptracks, more work is required to establish whether it is an accurate measure of aerosol-limited conditions, particularly in regions far from existing clouds.

3.2 Microphysics

The previous section has shown that the background meteorological state has a controlling influence on the macrophysical properties of shiptracks and their sensitivity to aerosol. These are not independent from the microphysical properties of the shiptrack, particularly the ε_N, which is closely related to shiptrack detection. Changes in the microphysics can also have a distinct impact on the potential radiative forcing from shiptracks. In this section, the changes in the N_d and LWP are examined to investigate these controls in more depth and quantify the radiative response as a function of time.

3.2.1 Polluted vs. detected

Detected pixels (more than 2 standard deviations above the background N_d) are only a subset of the pixels within the shiptrack. In this section, the "polluted" N_d (Fig. 1) is used as a measure of the N_d within the shiptrack, enabling a consistent comparison between segments with and without a detected shiptrack. The detected ε_N is positive by definition (Fig. 8a). As it includes (undetected) pixels with a lower N_d, the polluted N_d is smaller than the detected N_d and in some cases can lead to an ε_N of less than one (typically in segments where there are no detected pixels).

In segments where both the polluted and detected N_d exist, there is a close correlation between the polluted and detected ε_N (r=0.9; Fig. 8b). This correlation rises further (to 0.95), when only segments with more than five detected pixels are included,
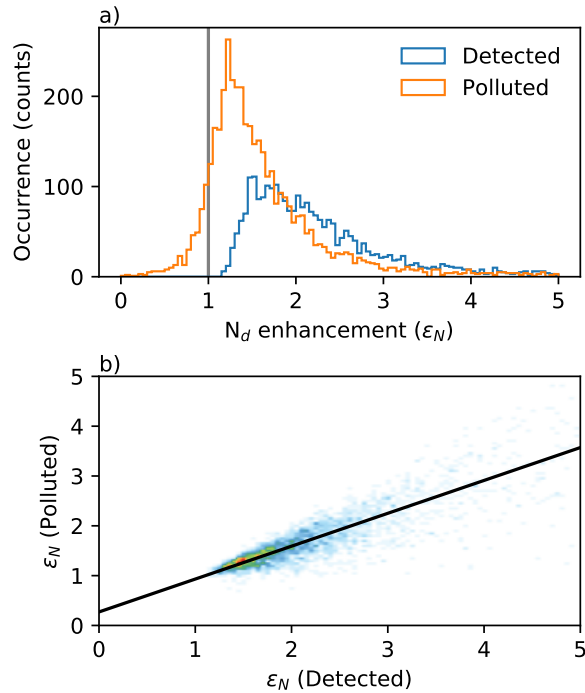
Figure 8. a) The N_d enhancement (ε_N) for detected cases and all polluted cases two to three hours after emission for all cases with sufficient cloud. b) the relationship between polluted and detected for all cases in (a) where both metrics are derived.

indicating that the primary source of uncertainty is in the detected ε_N. This supports the use of the polluted ε_N for characterising the shiptracks in this work.

3.2.2 N_d development

Previous studies have shown a strong link between the ship emissions and the detected ε_N (Gryspeerdt et al., 2019b). This
5   enhancement peaks in the early stages of the shiptrack formation and decreases quickly with time (Fig. 9a). As it depends on the relatively small number of detected pixels, the uncertainty in the enhancement is relatively high and the difference between the high and low SO_x ships becomes small after five hours. Part of this uncertainty is due to a sampling effect, as weak ε_N segments have no detected pixels and so are excluded from the calculation. This means that the average enhancement tends towards the lowest detectable enhancement.

10   A clearer signal is found using the polluted ε_N (Fig. 9b). Following a quick increase in ε_N during the shiptrack formation, a maximum is reached within about one hour (similar to the formation timescale in Fig. 3c). This timescale is longer than the formation timescale for the detected ε_N (Fig. 9a), as the detected ε_N only includes clouds where the ship SO_x emissions have already had a detectable impact. The polluted ε_N is almost 50% larger for ships with higher SO_x emissions ($>0.13\,\mathrm{kg\,s^{-1}}$) than lower emissions, a difference maintained until more than 10 hours since emission. The decrease in ε_N with time emphasises the
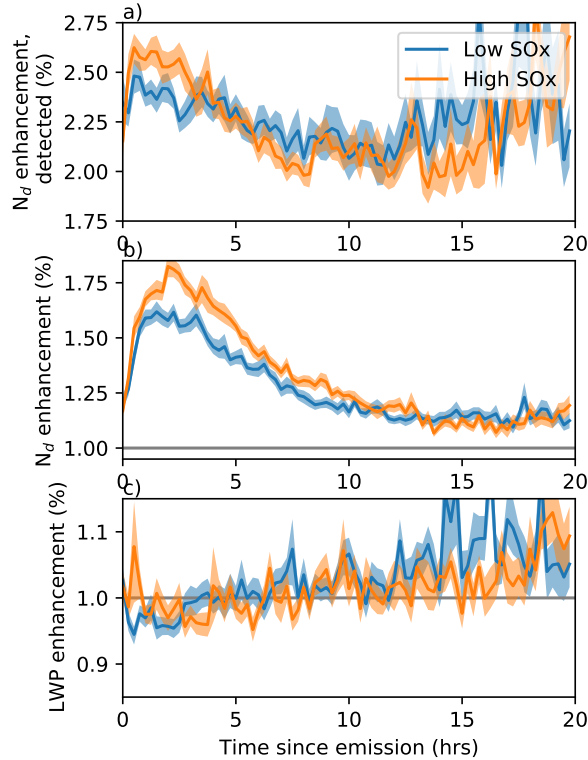
Figure 9. a) The change in ε_N for detected pixels only as a function of time from emission, for low and high SO$_x$ emitting ships respectively. b), as (a), but including all the pixels within the shiptrack as the polluted pixels. c) As (b), but for the LWP instead of the N_d.

importance of temporal development when considering aerosol impacts on clouds, especially those from an isolated aerosol source where there is no replenishment of the aerosol. This also demonstrates that if time since emission is not accounted for, the ε_N (detected or polluted) is not a good measure of the aerosol perturbation.

Although noisy, some patterns can be observed in the LWP enhancement ($\varepsilon_L = \frac{LWP_{pol}}{LWP_{cln}}$; Fig. 9c). There is an initial decrease

5   of approximately 5% in the ε_L, followed by an increase in the ε_L after two hours, becoming positive (increased LWP inside the shiptrack) at around seven hours since emission. There is no clear difference in ε_L between ships with high and low SO$_x$ emissions.

3.2.3   Meteorology and N_d development

As well as being a clear function of time, the ε_N is also a function of meteorological state, such that even the ε_N at a given

10   time since emission is not necessarily a good measure of the aerosol perturbation. As the meteorological conditions can change along the length of a shiptrack, the results in the following sections are composited, with the meteorological conditions being
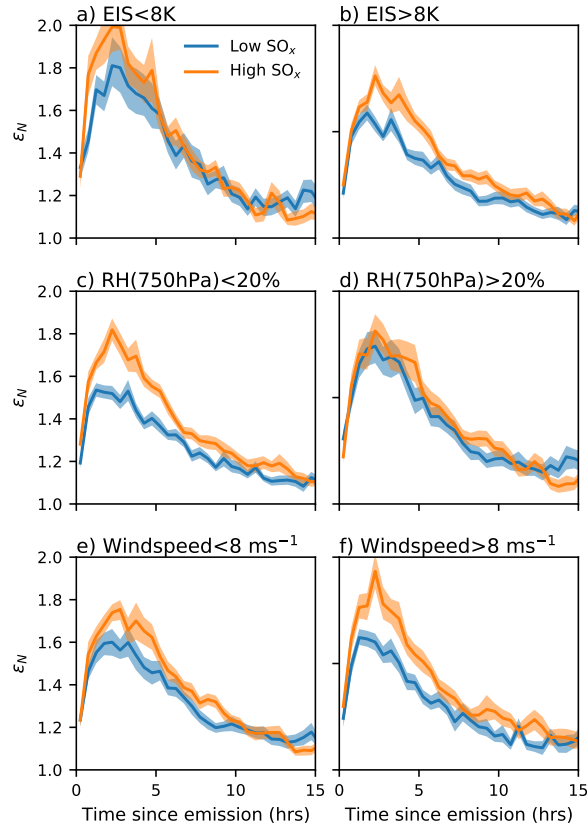
Figure 10. As Fig. 9b, but stratified by: a,b) estimated inversion strength (EIS), c,d) relative humidity at 750 hPa, e,f) 1000 hPa windspeed. Orange and blue are high and low SO_x emissions respectively.

calculated independently for each segment along the track. This allows situations where a track transects a region of variable meteorological conditions to be investigated.

The ε_N is higher at low EIS (Fig. 10a), where it is also sensitive to ship SO_x emissions with increased SO_x enhancing the ε_N further. However, the ε_N for both the high and low SO_x tracks becomes very similar after four hours. This is similar to the track length in Fig. 6b, which is also not a strong function of the aerosol perturbation. In both cases, the impact of meteorological variations dominates the variability from the magnitude of the aerosol perturbation. In contrast, while the ε_N is smaller (partially due to a larger N_{cln}; Bennartz and Rausch, 2017) in the high EIS cases (Fig. 10b), the signal from the aerosol perturbation remains to almost 20 hours (although the ε_N itself is still a strong function of time).

Relative humidity also affects ε_N, with shiptracks at lower cloud top humidity being more sensitive to the initial aerosol perturbation (Fig. 10c). When the cloud top humidity is higher, the sensitivity of the ε_N to the aerosol perturbation disappears almost entirely (Fig. 10d). This is expected following previous work showing shiptracks are more likely to form in regions

with a low cloud top humidity (Gryspeerdt et al., 2019b), potentially due to the increased cloud top cooling promoting strong updraughts and so a larger sensitivity to aerosol (Lilly, 1968).

The dependence of the ε_N development on surface windspeed may have a similar origin. The larger sensitivity of ε_N to the aerosol perturbation at higher windspeeds (Fig. 10f) may be due to the increased surface fluxes promoting a larger in-cloud
5   updraught and hence a more aerosol-limited environment.

3.2.4 LWP sensitivity
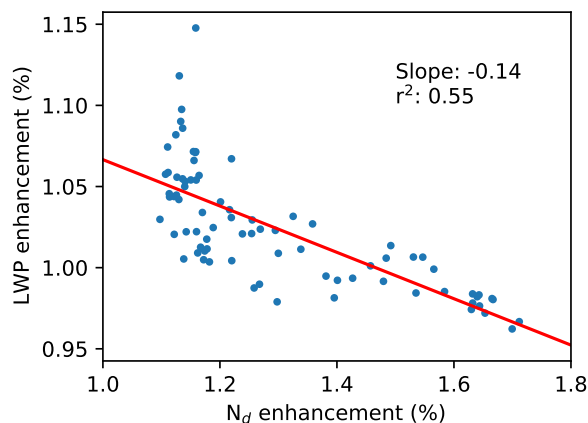
Figure 11. The relationship between the mean LWP and N_d enhancements in Fig. 9. The slope and r^2 values for a linear regression are given in the plot.

The impact of aerosol on the liquid water path is often quantified as the sensitivity of LWP to N_d, $\frac{d\ln LWP}{d\ln N_d} = \frac{\ln \varepsilon_L}{\ln \varepsilon_N}$ (e.g. Han et al., 2002; Feingold, 2003). This sensitivity can be calculated directly from a shiptrack, comparing the polluted and corresponding clean regions, and has been used to quantify the strength of LWP adjustments to aerosol (e.g. Toll et al., 2019).
10   However, the temporal development in ε_L and ε_N (Figs. 9b,c) will generate a negative bias to the N_d-LWP sensitivity if the time since emission is not accounted for (Fig. 11). This negative relationship is driven primarily by the different timescales of the LWP and N_d response and could occur even if aerosol produced a strong LWP increase, highlighting the difficulties of using ε_N as a measure of the aerosol perturbation without accounting for the temporal development of the perturbation..

To include this development, the average sensitivity (calculated individually for each segment using the ε_L and polluted ε_N)
15   is shown as function of time from emission in Fig. 12a. Considering all the shiptracks together (blue line), the sensitivity almost instantaneously decreases to -0.1, before slowly decreasing to -0.2 over the following 15 hours. Using N_{cln}, as a measure of the background cloud state (e.g. Gryspeerdt et al., 2019b), it is seen that not only is the sensitivity a function of time since emission, it is a strong function of N_{cln} (Fig. 12a). A bi-directional LWP response has been observed in several previous studies (Han et al., 2002; Chen et al., 2012; Gryspeerdt et al., 2019a; Toll et al., 2019), hypothesised to be a combination of
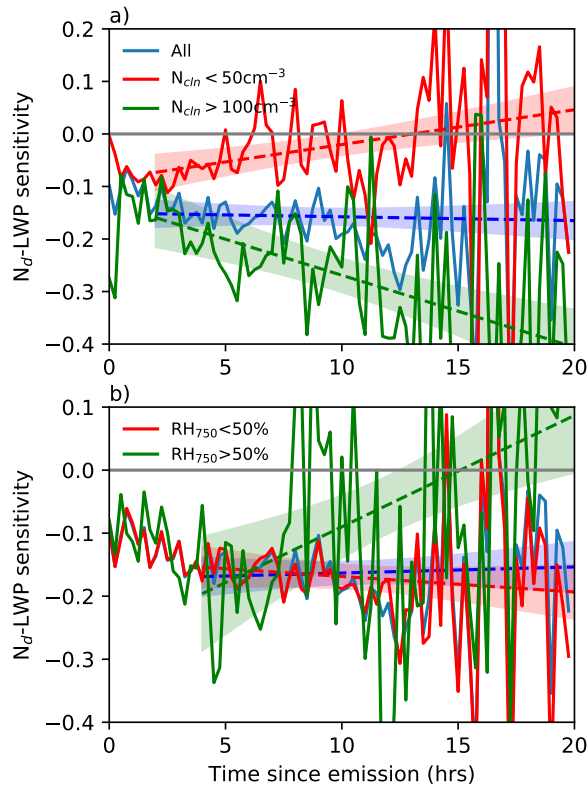
Figure 12. The LWP sensitivity to N_d as a function of time since emission. a) shows the development of the sensitivity as a function of N_{cln}, b) as a function of RH(750hPa). The blue line is the same in both plots as a reference. Linear fits for the data from 2 to 10 hours after emission, along with a standard error on the fit are also shown.

precipitation suppression (generating a positive sensitivity of LWP to N_d) and aerosol dependent entrainment (generating a negative sensitivity Ackerman et al., 2004).

This bi-directional LWP sensitivity response is clear in (Fig. 12a). For both the clean and polluted background clouds, the sensitivity is initially very similar, beginning to diverge after two hours and produce a more positive sensitivity in cleaner
5   background conditions. This is consistent with the precipitation suppression effect dominating in clean regions, but the enhanced entrainment being more important for polluted situations (e.g. Gryspeerdt et al., 2019a). This behaviour continues to at least 20 hours since emission, although the sensitivities at long timescales should be treated with some caution due to the small number of shiptracks remaining at such long times. The exact values of the sensitivity at large times since emission also depend significantly on the choices made in the shiptrack pixel identification algorithm, although the qualitative results remain.
10   At long timescales, the sensitivity would tend towards to the large scale statistics, which may be impacted by retrieval biases from correlated errors in the LWP and N_d retrievals (Gryspeerdt et al., 2019a).

A similar divergence in the sensitivity is observed as a function of cloud top humidity (Fig. 12b). Both dry and moist cloud-top conditions maintain a similar sensitivity for the first four hours; at subsequent times, the more humid cloud tops have a more positive sensitivity, increasing over time. This is consistent with the impact of humidity through cloud top entrainment shown in previous studies (Ackerman et al., 2004; Toll et al., 2019).

5   While these results support those found in previous studies, there are a number of important factors that must be taken into account when interpreting those studies. First, as demonstrated in model studies (Glassmeier et al., 2021), the N_d-LWP sensitivity is not constant with time. This introduces extra uncertainties into studies that do not account for this variation. Second, ε_N is a poor indicator of the aerosol perturbation under some meteorological conditions (Fig. 10). If the ε_N is primarily a factor of the local meteorology, this increases the potential impact of meteorological covariations on the sensitivity (e.g.

10   Gryspeerdt et al., 2019a). Finally, the timescales involved may hint at the potential for a retrieval bias creating an extra negative sensitivity in these results (see Sec. 4.2).

3.2.5   LWP development

Averaging the changes in LWP over hour-long periods, the temporal changes in LWP after the aerosol emission become clearer (Fig. 13). A decrease in LWP is observed at short timescales, followed by an increase in LWP at longer timescales (Wang and

15   Feingold, 2009b). There is no clear difference in LWP evolution for the high or low SO_x emissions.

   As seen in the sensitivity, when looking at cases with a clean background (Fig. 13b), after a short term decrease in LWP, there is a strong increase in LWP after 5 hours since emission. This is likely due to precipitation suppression and the circulation adjustments created around a spatially limited aerosol perturbation (Scorer, 1987; Wang and Feingold, 2009b), particularly in an open-celled stratocumulus regime (Christensen and Stephens, 2011).

20   For shiptracks forming in polluted environments, there is a small decrease in LWP (Fig. 13c). This decrease is larger for shiptracks formed by larger SO_x emissions, although the overall magnitude of the effect is smaller than the increase in cleaner conditions. Although the sensitivity appears to continue to increase, the near constant ε_L (Fig. 13c) appears to suggest that the increase in sensitivity is almost exactly offset by the decrease in ε_N. This is in contrast to the results from (Glassmeier et al., 2021), which suggests that the change in sensitivity comes from the LWP adjusting to the change in N_d. Further work

25   is required to properly understand to what extent shiptracks and the response to isolated pollution sources represent the actual response of cloud and particularly LWP to aerosol perturbations.

4   Discussion

4.1   Potential radiative forcing

The combination of these increases in N_d (Fig. 10), LWP (Fig. 13) and CF (Fig. 7) produce an increase in reflected shortwave

30   radiation, providing a way to compare the different perturbations with a similar metric. Integrating the potential radiative forcing along each shiptrack before creating a composite shows that about half the total radiative impact of the composite
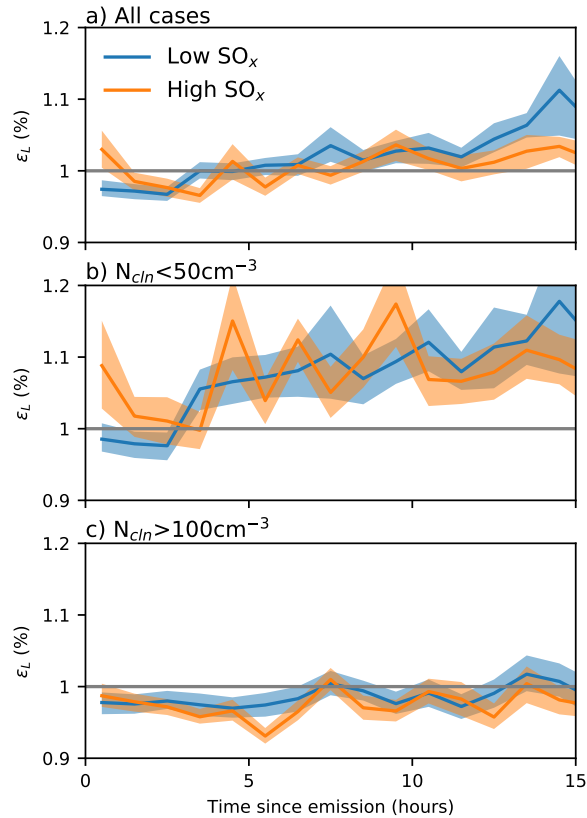
Figure 13. Development of LWP along shiptracks for all ships (a). b) clean background environments (N_{cln} <50cm^{-3}). c) polluted background environments (N_{cln} >100cm^{-3}).

shiptrack comes in the first five hours (Fig. 14a). During this period, the SO$_x$ emissions of the ship do not have a strong impact on the integrated forcing. The SO$_x$ impact increases in the later stages of the shiptrack lifetime, where higher SO$_x$ emitting ships produce a larger ε_N (Fig. 9b) later in their lifetimes. Excluding the CF change (Fig. 14d) shows that approximately half the total radiative effect of the shiptrack comes from CF increases. The weak correlation of these CF increases to the ship SO$_x$

5 emissions explains the insensitivity of the integrated forcing to SO$_x$ during the early stages of the track.

The liquid cloud fraction has previously been shown to be the primary control on shiptrack formation (Gryspeerdt et al., 2019b). This is strongly linked to the EIS, with more liquid cloud in more stable environments (Wood and Bretherton, 2006). However, despite a higher cloud fraction at high EIS, shiptracks formed in lower EIS environments have a larger radiative effect (Fig. 14b). This is partly due to the lower CF allowing the CF (and hence forcing) to increase within the shiptrack.

10 With a higher background CF, there is less scope for a forcing due to a CF increase (Goren et al., 2019). This interpretation is supported by the results at a constant cloud fraction (Fig. 14e), where after an initial difference in the forcing (due to the higher ε_N at low EIS; Fig. 10), the integrated forcing for the high and low EIS populations is very similar after ten hours.
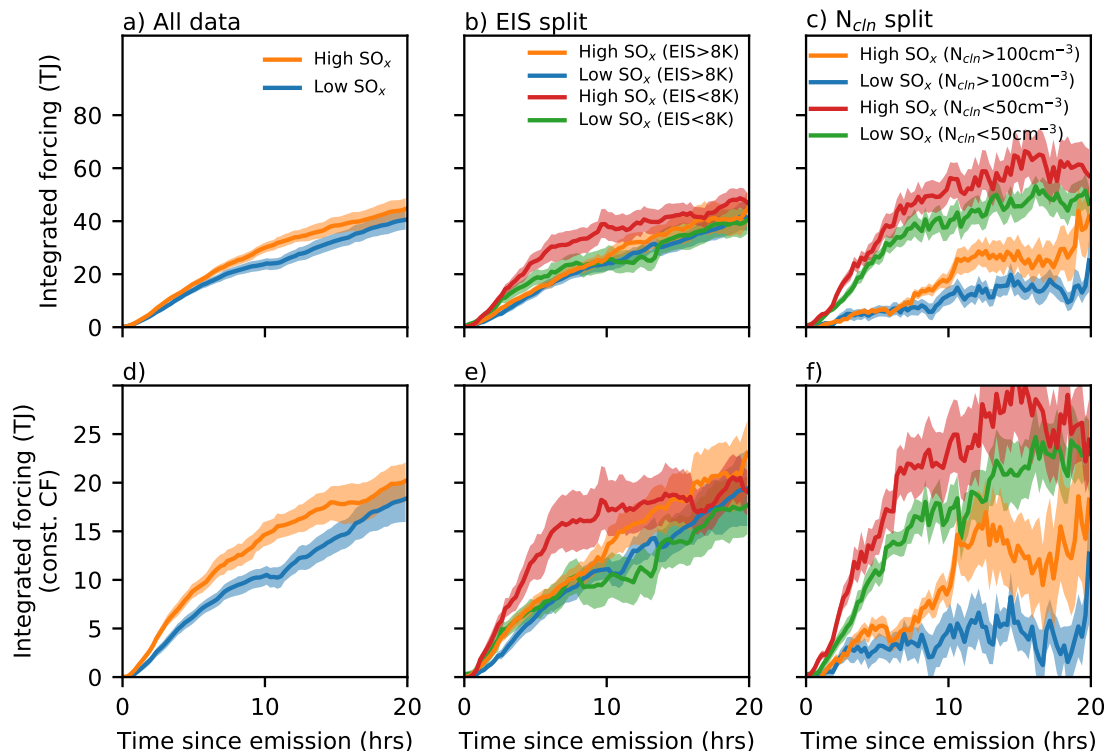
Figure 14. The integrated potential forcing as a function of time since emission including (top row) and excluding (bottom row) CF changes (Eq. (1)). Note the different scales. a,d) All shiptracks, separated by high and low SO_x emissions. b,e) Separated by high and low SO_x emissions for high EIS (>8K; orange and blue) and low EIS (<8K, red and green as high and low SO_x respectively). c,f) As (b) and (d), but for high N_{cln} (>100cm^{-3}; orange and blue) and low N_{cln} (<50cm^{-3}; red and green).

Although EIS has some control over the radiative effect of shiptracks, background N_d have the largest impact on shiptrack radiative properties (Fig. 14c), with larger ε_N (Gryspeerdt et al., 2019b), ε_L (Fig. 13) and CF enhancement (Fig. 7) occurring with a clean background. The forcing for the clean background (N_{cln} <50cm^{-3}) cases is mostly within the first seven hours, with very little increase in the integrated forcing after this time. This is likely due to the lower cloud fraction at a lower
5 N_{cln} (Gryspeerdt et al., 2016) both enhancing the forcing from CF increases in the early stages of the track and limiting the forcing from ε_N increases in the later stages. In contrast, the integrated forcing from shiptracks in polluted backgrounds shows a relatively steady increase with time, although after twenty hours it still has less than half the integrated forcing of the shiptracks in clean environments. These shiptrack locations were only estimated up to twenty hours from emission. Some very long-lived shiptracks have radiative impacts lasting several days (Goren and Rosenfeld, 2012), which would lead to significant changes
10 at longer timescales.

4.2 Timescales

The N_d response to the aerosol perturbation proceeds at a timescale approximating a boundary layer mixing timescale of around half an hour (Figs. 3d, 9). The timescale for the precipitation suppression impact on LWP to become clear is around two hours (Fig. 12a). This increase in LWP is quicker than the four hour delay in Wang and Feingold (2009b) but slower than the almost instantaneous LWP response to a N_d increase in Feingold et al. (2015). It may also indicate that the LWP response to precipitation/circulation effects is faster than model simulations suggest.

The aerosol impact through a modification of entrainment proceeds at a slower pace. In Fig. 12b, it taking more than four hours for the impact of variations in cloud top humidity to begin to appear. As the impact of cloud top entrainment depends on the humidity, the timescale for humidity variations to impact the N_d-LWP sensitivity is the relevant timescale for the impact of aerosol-dependent entrainment. This compares well with the results from Glassmeier et al. (2021), which shows a characteristic timescale for the LWP adjustment via entrainment of 20 hours, which produces a 20% of the total change after four hours.

While these timescales match previous work, the N_d-LWP sensitivity adjusts very quickly immediately behind the ship (Fig. 12). The sensitivity reaches -0.1 within the first 15 minutes, meaning that the LWP has changed on the same timescale as the N_d. While the N_d can respond at this timescale (e.g. Wang and Feingold, 2009b), LWP adjustments depending on precipitation or entrainment appear to operate at longer timescales (Fig. 12). An increased droplet surface area and so condensation rate could produce a fast change to the LWP, but would lead to LWP increases (Koren et al., 2014).

An r_e retrieval bias may also be the cause of this near instant LWP adjustment. Both the LWP and N_d are calculated using the cloud optical depth and r_e, so random errors in the r_e become correlated errors in the LWP and N_d, generating a negative sensitivity bias (e.g. Gryspeerdt et al., 2019a). Retrieval biases are insensitive to the time since emission and so would be capable of producing this almost instant LWP adjustment.

One potential cause of an r_e retrieval bias could be in the droplet size distribution (DSD) (Painemal and Zuidema, 2011). The shape of the DSD affects the relative number of small and large droplets and hence the link between the N_d and r_e. Aircraft studies have shown a wider DSD in shiptracks compared to the surrounding cloud, which would create an uncertainty in retrieval of cloud properties in shiptracks (Noone et al., 2000). Future high spatial-resolution polarimeters may be able to resolve this ambiguity.

If the initial value of the sensitivity of -0.1 represents the impact of retrieval biases, this suggests the negative sensitivities determined from previous studies of shiptracks should be smaller, resulting in a weaker LWP reduction in response to aerosol. Recent studies have suggested that the LWP adjustments inferred from shiptracks may be underestimated due to the lack of consideration of the shiptrack temporal development (Glassmeier et al., 2021). These model results are supported by the observational evidence presented in this work (Fig. 12), suggesting that the long term LWP sensitivity to N_d may be larger than found in previous studies. It should be noted that the long-term temporal development of these shiptracks (particularly those that contain no detected pixels), will tend to the large-scale statistics, which themselves may be subject to biases from correlated errors (e.g. Gryspeerdt et al., 2019a). However, these two factors suggest that the interpretation of current and future

studies inferring LWP adjustments from natural experiments should consider the temporal development of the perturbation and the possibility of retrieval errors.

4.3 Future improvements

This work has shown that many shiptrack properties vary significantly along the length of the track. As shiptracks do not transmit information along their length, they can be considered a collection of semi-independent segments, with the same initial aerosol perturbation, but at different times since emission. Using the ship location and the local windfield for reanalysis, the time since emission is inferred, allowing the timescales of the relevant cloud and aerosol processes to be measured. However, the results in this work come with some caveats.

The MODIS images are still only a snapshot of the cloud field, such that the time axis determined from the ship and cloud motion is not a real time axis. The unperturbed clouds will also develop over the time period (Christensen et al., 2009; Kabatas et al., 2013), such that the "unperturbed" clouds here are not a true measure of the cloud at the time of the aerosol perturbation. The polluted clouds will also have evolved, not necessarily in the same manner. The climatological meteorological fields also affect both the clean and polluted clouds (15 hours can be several hundred kilometres). This generates uncertainties that will be resolved in future work through the use of geostationary observations.

Although many shiptracks are intersected by CloudSat/CALIPSO, it is not enough to build up a picture of the precipitation development in these shiptracks. MODIS views every segment in each track, with 1,209 tracks, almost 100,000 segments are used in this study. CloudSat will typically only view one segment per track (if any), so that resolving the development to the same detail requires 80 times as many shiptracks. Expanding this work to a global scale will not only allow the inclusion of other regions for shiptrack formation (Schreier et al., 2007), but will enable a more complete picture of the factors limiting and controlling aerosol perturbations on cloud properties.

This study uses N_d to locate shiptracks, in contrast to earlier work that used near-IR reflectance (Segrin et al., 2007, e.g.). This increases the contrast and hence detectability of shiptracks in cloud-covered scenes and case where there is no change in r_e (see S.I.). This comes at a cost of a reduced shiptrack detection efficiency in scenes with low numbers of successful liquid cloud retrievals. A more effective combination of the information from these two sources would lead to a more complete sample of shiptracks in a wide variety of background conditions.

5 Conclusions

Cloud responses to aerosol perturbations are not instant, but instead develop over characteristic timescales. This work uses ship position information and reanalysis windfields to develop a time-axis for satellite-observed shiptracks, providing a method for measuring the timescales of aerosol-cloud interactions from individual satellite images. The advected emission locations also provide an estimate for shiptrack locations in regions where they are too weak to be detected by existing methods (Fig. 2).

While ships with higher SO_x emissions typically produce longer shiptracks, the median lifetime of the shiptracks studied in this work is not a strong function of the ship emissions (Fig. 3). The role of ship emissions for shiptrack length varies

by meteorological background, with shorter shiptracks being found in more unstable (higher EIS environments), where the shiptrack length is insensitive to the ship SO_x emissions (Fig. 6b). In contrast, higher SO_x emissions lead to a significant increase in track lifetime in more stable environments, due to the higher cloud fraction and stronger role for dissipation. Across their lifetime, a lack of cloud and insufficient N_d perturbations have approximately an equal role is shiptrack disappearance (Fig. 4).

After an initial increase in track width (within the first five hours), track width is relatively insensitive to the time since emission (Fig. 5). In high CF environments (an indicator of closed cells/sea fog), the track width increases with SO_x emissions. In low CF environments (indicating open cells), the track width is largely independent of SO_x as the track width is largely controlled by the cell width (Scorer, 1987).

The reanalysis windfield is used to locate shiptracks in otherwise cloud-free environments (Fig. 7). A significant increase in CF is found during the first 10 hours of the shiptrack lifetime, suggesting that around 5% of clear sky cases in this region are aerosol-limited (Fig. 7e). There is a large uncertainty on this number, due to potential random fluctuations in the cloud fraction retrievals. Further studies are required to establish the extent of these aerosol-limited cases across the global oceans.

The microphysical properties of the shiptrack, particularly the N_d enhancement (ε_N), along with the LWP enhancement also vary significantly with time since emission (Fig. 9). The ε_N quickly reaches a maximum around an hour after emission, before slowly decreasing. The strength of the ε_N maximum and its sensitivity to SO_x depend on the meteorological state, although cases with the largest ε_N (such as at low EIS; Fig. 10a), often have a lower sensitivity to the SO_x emissions (such as when the cloud top relative humidity is larger than 20%). The ε_N sensitivity to SO_x can persist over several hours. In high EIS situations, shiptracks produces by high SO_x ships still have a larger ε_N after 10 hours (Fig. 10b).

While the ε_N is correlated to SO_x in some cases, it is not a good measure of the aerosol perturbation, especially if the time since emission is not accounted for. The LWP enhancement (ε_L) increases over time (Fig. 9), such that ε_N and $\mathscr{L}$ temporal development create a negative N_d-LWP sensitivity in shiptracks, even if aerosols produced an increase in LWP (Fig. 11). Even when accounting for the shiptrack development, the N_d-LWP sensitivity remains strongly dependent on the time since emission, along with the background cloud and meteorological state (Fig. 12). After two hours, positive sensitivities become visible in clean cases and a dependence on the cloud top humidity appears after around four hours. These timescales are related to cloud processes (e.g. Feingold et al., 2015; Glassmeier et al., 2021), but the near-instant appearance of the negative sensitivity (within 15 min; Fig. 12) hints at a potential retrieval error. Correlated errors in the N_d and LWP retrievals are one possible explanation, perhaps caused by a change in the shape of the droplet size distribution (Noone et al., 2000), although in-situ studies are required to investigate this possibility. This temporal development of the N_d-LWP should be accounted for in studies of cloud adjustment to aerosol.

When combined, the radiative impact of the shiptracks investigated in this work is concentrated in the first 5-10 hours after emission (Fig. 14), with approximately half of the overall effect being due to the increase in CF in the early stages of the ship-track lifetime. This emphasises the large potential role of cloud fraction adjustments to the overall potential radiative forcing (Goren and Rosenfeld, 2014). This strong impact of the CF increase means that shiptracks in lower EIS environments have

a higher potential radiative forcing (Fig. 14b), although the background N_d dominates, with shiptracks in clean environments producing a four times larger integrated radiative forcing over the 20 hour study period.

Although uncertainties remain, this study demonstrates how isolated aerosol perturbations can be used to measure the timescales of aerosol impacts on cloud properties, showing that the N_d perturbation is not often a good measure of the size of the aerosol perturbation and that meteorology and background cloud state have an important role in determining the sensitivity of cloud properties to aerosol. Together, the results in this work emphasise the importance of accounting for time when using observations of isolated aerosol perturbations to constrain aerosol-cloud interactions.

Competing interests. The authors have no competing interests.

Acknowledgements. Ship emissions were derived using location data from ExactEarth. EG was supported by a Royal Society University Research Fellowship (URF/R1/191602). TG was funded by the European Union's Horizon 2020 Research and Innovation Programme under Grant Agreement 821205 (FORCeS)

References

Ackerman, A. S., Toon, O. B., and Hobbs, P. V.: Dissipation of Marine Stratiform Clouds and Collapse of the Marine Boundary Layer Due to the Depletion of Cloud Condensation Nuclei by Clouds, Science, 262, 226–229, https://doi.org/10.1126/science.262.5131.226, 1993.

Ackerman, A. S., Kirkpatrick, M. P., Stevens, D. E., and Toon, O. B.: The impact of humidity above stratiform clouds on indirect aerosol climate forcing, Nature, 432, 1014, https://doi.org/10.1038/nature03174, 2004.

Albrecht, B. A.: Aerosols, Cloud Microphysics, and Fractional Cloudiness, Science, 245, 1227–1230, https://doi.org/10.1126/science.245.4923.1227, 1989.

Bennartz, R. and Rausch, J.: Global and regional estimates of warm cloud droplet number concentration based on 13 years of AQUA-MODIS observations, Atmos. Chem. Phys., 17, 9815–9836, https://doi.org/10.5194/acp-17-9815-2017, 2017.

Bohren, C. F.: Multiple scattering of light and some of its observable consequences, Am. J. Phys., 55, 524, https://doi.org/10.1119/1.15109, 1987.

Boucher, O., Randall, D. A., Artaxo, P., Bretherton, C., Feingold, G., Forster, P. M., Kerminen, V.-M., Kondo, Y., Liao, H., Lohmann, U., Rasch, P., Satheesh, S. K., Sherwood, S., Stevens, B., and Zhang, X. Y.: Clouds and Aerosols, Cambridge University Press, https://doi.org/10.1017/CBO9781107415324.016, 2013.

Bretherton, C. S., Blossey, P. N., and Uchida, J.: Cloud droplet sedimentation, entrainment efficiency, and subtropical stratocumulus albedo, Geophys. Res. Lett., 34, https://doi.org/10.1029/2006GL027648, 2007.

Chen, Y.-C., Christensen, M. W., Xue, L., Sorooshian, A., Stephens, G. L., Rasmussen, R. M., and Seinfeld, J. H.: Occurrence of lower cloud albedo in ship tracks, Atmos. Chem. Phys., 12, 8223–8235, https://doi.org/10.5194/acp-12-8223-2012, 2012.

Christensen, M. W. and Stephens, G. L.: Microphysical and macrophysical responses of marine stratocumulus polluted by underlying ships: Evidence of cloud deepening, J. Geophys. Res., 116, D03 201, https://doi.org/10.1029/2010JD014638, 2011.

Christensen, M. W., Coakley, J. A., and Tahnk, W. R.: Morning-to-Afternoon Evolution of Marine Stratus Polluted by Underlying Ships: Implications for the Relative Lifetimes of Polluted and Unpolluted Clouds, J. Atmos. Sci., 66, 2097–2106, https://doi.org/10.1175/2009JAS2951.1, 2009.

Christensen, M. W., Jones, W. K., and Stier, P.: Aerosols enhance cloud lifetime and brightness along the stratus-to-cumulus transition, P. Natl. Acad. Sci. USA, 117, 17 591–17 598, https://doi.org/10.1073/pnas.1921231117, 2020.

Conover, J. H.: Anomalous Cloud Lines, J. Atmos. Sci., 23, 778–785, https://doi.org/10.1175/1520-0469(1966)023<0778:ACL>2.0.CO;2, 1966.

Durkee, P. A., Chartier, R. E., Brown, A., Trehubenko, E. J., Rogerson, S. D., Skupniewicz, C., Nielsen, K. E., Platnick, S., and King, M. D.: Composite Ship Track Characteristics, J. Atmos. Sci., 57, 2542–2553, https://doi.org/10.1175/1520-0469(2000)057<2542:CSTC>2.0.CO;2, 2000a.

Durkee, P. A., Noone, K. J., Ferek, R. J., Johnson, D. W., Taylor, J. P., Garrett, T. J., Hobbs, P. V., Hudson, J. G., Bretherton, C. S., Innis, G., Frick, G. M., Hoppel, W. A., O'Dowd, C. D., Russell, L. M., Gasparovic, R., Nielsen, K. E., Tessmer, S. A., Öström, E., Osborne, S. R., Flagan, R. C., Seinfeld, J. H., and Rand, H.: The Impact of Ship-Produced Aerosols on the Microstructure and Albedo of Warm Marine Stratocumulus Clouds: A Test of MAST Hypotheses 1i and 1ii., J. Atmos. Sci., 57, 2554–2569, https://doi.org/10.1175/1520-0469(2000)057<2554:TIOSPA>2.0.CO;2, 2000b.

Efron, B.: Bootstrap methods: Another look at the jackknife, Ann. Stat., 7, 1–26, 1979.

Feingold, G.: First measurements of the Twomey indirect effect using ground-based remote sensors, Geophys. Res. Lett., 30, 1287, https://doi.org/10.1029/2002GL016633, 2003.

Feingold, G., Koren, I., Wang, H., Xue, H., and Brewer, W. A.: Precipitation-generated oscillations in open cellular cloud fields, Nature, 466, 849–852, https://doi.org/10.1038/nature09314, 2010.

Feingold, G., Koren, I., Yamaguchi, T., and Kazil, J.: On the reversibility of transitions between closed and open cellular convection, Atmos. Chem. Phys., 15, 7351–7367, https://doi.org/10.5194/acp-15-7351-2015, 2015.

Glassmeier, F., Hoffmann, F., Johnson, J. S., Yamaguchi, T., Carslaw, K. S., and Feingold, G.: Aerosol-cloud-climate cooling overestimated by ship-track data, Science, 371, 485–489, https://doi.org/10.1126/science.abd3980, 2021.

Goren, T. and Rosenfeld, D.: Satellite observations of ship emission induced transitions from broken to closed cell marine stratocumulus over large areas, J. Geophys. Res., 117, 17 206, https://doi.org/10.1029/2012JD017981, 2012.

Goren, T. and Rosenfeld, D.: Decomposing aerosol cloud radiative effects into cloud cover, liquid water path and Twomey components in marine stratocumulus, Atmos. Res., 138, 378–393, https://doi.org/10.1016/j.atmosres.2013.12.008, 2014.

Goren, T., Kazil, J., Hoffmann, F., Yamaguchi, T., and Feingold, G.: Anthropogenic Air Pollution Delays Marine Stratocumulus Breakup to Open Cells, Geophys. Res. Lett., 46, 14 135–14 144, https://doi.org/10.1029/2019GL085412, 2019.

Grosvenor, D. P., Sourdeval, O., Zuidema, P., Ackerman, A., Alexandrov, M. D., Bennartz, R., Boers, R., Cairns, B., Chiu, J. C., Christensen, M., Deneke, H., Diamond, M., Feingold, G., Fridlind, A., Hünerbein, A., Knist, C., Kollias, P., Marshak, A., McCoy, D., Merk, D., Painemal, D., Rausch, J., Rosenfeld, D., Russchenberg, H., Seifert, P., Sinclair, K., Stier, P., van Diedenhoven, B., Wendisch, M., Werner, F., Wood, R., Zhang, Z., and Quaas, J.: Remote Sensing of Droplet Number Concentration in Warm Clouds: A Review of the Current State of Knowledge and Perspectives, Rev. Geophys., https://doi.org/10.1029/2017RG000593, 2018.

Gryspeerdt, E., Stier, P., and Partridge, D. G.: Satellite observations of cloud regime development: the role of aerosol processes, Atmos. Chem. Phys., 14, 1141–1158, https://doi.org/10.5194/acp-14-1141-2014, 2014.

Gryspeerdt, E., Quaas, J., and Bellouin, N.: Constraining the aerosol influence on cloud fraction, J. Geophys. Res., 121, 3566–3583, https://doi.org/10.1002/2015JD023744, 2016.

Gryspeerdt, E., Goren, T., Sourdeval, O., Quaas, J., Mülmenstädt, J., Dipu, S., Unglaub, C., Gettelman, A., and Christensen, M.: Constraining the aerosol influence on cloud liquid water path, Atmos. Chem. Phys., 19, 5331–5347, https://doi.org/10.5194/acp-19-5331-2019, 2019a.

Gryspeerdt, E., Smith, T. W. P., O'Keeffe, E., Christensen, M. W., and Goldsworth, F. W.: The Impact of Ship Emission Controls Recorded by Cloud Properties, Geophys. Res. Lett., 46, 12 547–12 555, https://doi.org/10.1029/2019GL084700, 2019b.

Han, Q., Rossow, W. B., Zeng, J., and Welch, R.: Three Different Behaviors of Liquid Water Path of Water Clouds in Aerosol–Cloud Interactions, J. Atmos. Sci., 59, 726–735, https://doi.org/10.1175/1520-0469(2002)059<0726:TDBOLW>2.0.CO;2, 2002.

Jin, Z., Charlock, T. P., Smith, W. L., and Rutledge, K.: A parameterization of ocean surface albedo, Geophys. Res. Lett., 31, https://doi.org/10.1029/2004GL021180, 2004.

Kabatas, B., Menzel, W. P., Bilgili, A., and Gumley, L. E.: Comparing Ship-Track Droplet Sizes Inferred fromTerra and Aqua MODIS Data, J. Appl. Meteorol. Clim., 52, 230–241, https://doi.org/10.1175/JAMC-D-11-0232.1, 2013.

Koren, I., Feingold, G., and Remer, L. A.: The invigoration of deep convective clouds over the Atlantic: aerosol effect, meteorology or retrieval artifact?, Atmos. Chem. Phys., 10, 8855–8872, https://doi.org/10.5194/acp-10-8855-2010, 2010.

Koren, I., Dagan, G., and Altaratz, O.: From aerosol-limited to invigoration of warm convective clouds, Science, 344, 1143–1146, https://doi.org/10.1126/science.1252595, 2014.

Lehahn, Y., Koren, I., Altaratz, O., and Kostinski, A. B.: Effect of coarse marine aerosols on stratocumulus clouds, Geophys. Res. Lett., 38, L20 804, https://doi.org/10.1029/2011GL048504, 2011.

Lensky, I. M. and Rosenfeld, D.: Clouds-Aerosols-Precipitation Satellite Analysis Tool (CAPSAT), Atmos. Chem. Phys., 8, 6739–6753, https://doi.org/10.5194/acp-8-6739-2008, 2008.

5   Lilly, D. K.: Models of cloud-topped mixed layers under a strong inversion, Q. J. Roy. Meteor. Soc., 94, 292–309, https://doi.org/10.1002/qj.49709440106, 1968.

Liu, Q., Kogan, Y. L., Lilly, D. K., Johnson, D. W., Innis, G. E., Durkee, P. A., and Nielsen, K. E.: Modeling of Ship Effluent Transport and Its Sensitivity to Boundary Layer Structure, J. Atmos. Sci., 57, 2779–2791, https://doi.org/10.1175/1520-0469(2000)057<2779:MOSETA>2.0.CO;2, 2000.

10 Matsui, T., Masunaga, H., Kreidenweis, S. M., Pielke, R. A., Tao, W.-K., Chin, M., and Kaufman, Y. J.: Satellite-based assessment of marine low cloud variability associated with aerosol, atmospheric stability, and the diurnal cycle, J. Geophys. Res., 111, 17 204, https://doi.org/10.1029/2005JD006097, 2006.

McCoy, D. T., Bender, F. A.-M., Mohrmann, J. K. C., Hartmann, D. L., Wood, R., and Grosvenor, D. P.: The global aerosol-cloud first indirect effect estimated using MODIS, MERRA, and AeroCom, J. Geophys. Res., 122, 1779–1796, https://doi.org/10.1002/2016JD026141, 2017.

15 McCoy, D. T., Field, P., Gordon, H., Elsaesser, G. S., and Grosvenor, D. P.: Untangling causality in midlatitude aerosol–cloud adjustments, Atmos. Chem. Phys., 20, 4085–4103, https://doi.org/10.5194/acp-20-4085-2020, 2020.

Meskhidze, N., Remer, L. A., Platnick, S., Negrón Juárez, R., Lichtenberger, A. M., and Aiyyer, A. R.: Exploring the differences in cloud properties observed by the Terra and Aqua MODIS Sensors, Atmos. Chem. Phys., 9, 3461–3475, https://doi.org/10.5194/acp-9-3461-2009, 2009.

20 Muhlbauer, A., Ackerman, T. P., Comstock, J. M., Diskin, G. S., Evans, S. M., Lawson, R. P., and Marchand, R. T.: Impact of large-scale dynamics on the microphysical properties of midlatitude cirrus, J. Geophys. Res., 119, 3976–3996, https://doi.org/10.1002/2013JD020035, 2014.

Noone, K. J., Johnson, D. W., Taylor, J. P., Ferek, R. J., Garrett, T., Hobbs, P. V., Durkee, P. A., Nielsen, K., Öström, E., O'Dowd, C., Smith, M. H., Russell, L. M., Flagan, R. C., Seinfeld, J. H., de, B. L., van, G. R. E., Hudson, J. G., Brooks, I., Gasparovic, R. F., and Pockalny, R. A.: A Case Study of Ship Track Formation in a Polluted Marine Boundary Layer., J. Atmos. Sci., 57, 2748, https://doi.org/10.1175/1520-0469(2000)057<2748:ACSOST>2.0.CO;2, 2000.

Painemal, D. and Zuidema, P.: Assessment of MODIS cloud effective radius and optical thickness retrievals over the Southeast Pacific with VOCALS-REx in situ measurements, J. Geophys. Res., 116, D24 206, https://doi.org/10.1029/2011JD016155, 2011.

Platnick, S., Meyer, K. G., King, M. D., Wind, G., Amarasinghe, N., Marchant, B., Arnold, G. T., Zhang, Z., Hubanks, P. A., Holz, R. E., Yang, P., Ridgway, W. L., and Riedi, J.: The MODIS Cloud Optical and Microphysical Products: Collection 6 Updates and Examples From Terra and Aqua, IEEE T. Geosci. Remote, 55, 502–525, https://doi.org/10.1109/TGRS.2016.2610522, 2017.

Possner, A., Wang, H., Wood, R., Caldeira, K., and Ackerman, T. P.: The efficacy of aerosol–cloud radiative perturbations from near-surface emissions in deep open-cell stratocumuli, Atmos. Chem. Phys., 18, 17 475–17 488, https://doi.org/10.5194/acp-18-17475-2018, 2018.

Quaas, J., Boucher, O., and Lohmann, U.: Constraining the total aerosol indirect effect in the LMDZ and ECHAM4 GCMs using MODIS satellite data, Atmos. Chem. Phys., 6, 947–955, https://doi.org/10.5194/acp-6-947-2006, 2006.

Quaas, J., Stevens, B., Stier, P., and Lohmann, U.: Interpreting the cloud cover – aerosol optical depth relationship found in satellite data using a general circulation model, Atmos. Chem. Phys., 10, 6129–6135, https://doi.org/10.5194/acp-10-6129-2010, 2010.

Rosenfeld, D., Kaufman, Y. J., and Koren, I.: Switching cloud cover and dynamical regimes from open to closed Benard cells in response to the suppression of precipitation by aerosols, Atmos. Chem. Phys., 6, 2503–2511, https://doi.org/10.5194/acp-6-2503-2006, 2006.

Rosenzweig, M. R. and Wolpin, K. I.: Natural "Natural Experiments" in Economics, J. Econ. Lit., 38, 827–874, https://doi.org/10.1257/jel.38.4.827, 2000.

5 Schreier, M., Mannstein, H., Eyring, V., and Bovensmann, H.: Global ship track distribution and radiative forcing from 1 year of AATSR data, Geophys. Res. Lett., 34, 17 814, https://doi.org/10.1029/2007GL030664, 2007.

Scorer, R.: Ship trails, Atm. Env., 21, 1417–1425, https://doi.org/10.1016/0004-6981(67)90089-3, 1987.

Segrin, M. S., Coakley, J. A., and Tahnk, W. R.: MODIS Observations of Ship Tracks in Summertime Stratus off the West Coast of the United States, J. Atmos. Sci., 64, 4330, https://doi.org/10.1175/2007JAS2308.1, 2007.

10 Seifert, A., Heus, T., Pincus, R., and Stevens, B.: Large-eddy simulation of the transient and near-equilibrium behavior of precipitating shallow convection, J. Adv. Model. Earth Sy., 7, 1918–1937, https://doi.org/10.1002/2015MS000489, 2015.

Smith, T. W. P., Jalkanen, J. P., Anderson, B. A., Corbett, J. J., Faber, J., Hanayama, S., O'Keeffe, E., Parker, S., Johansson, L., Aldous, L., Raucci, C., Traut, M., Ettinger, S., Nelissen, D., Lee, D. S., Ng, S., Agrawal, A., Winebrake, J. J., Hoen, M., Chesworth, S., and Pandey, A.: The Third IMO GHG Study, International Maritime Organization (IMO), London, UK, 2015.

15 Toll, V., Christensen, M., Quaas, J., and Bellouin, N.: Weak average liquid-cloud-water response to anthropogenic aerosols, Nature, 572, 51–55, https://doi.org/10.1038/s41586-019-1423-9, 2019.

Twomey, S.: Pollution and the planetary albedo, Atmos. Environ., 8, 1251–1256, https://doi.org/10.1016/0004-6981(74)90004-3, 1974.

Wang, H. and Feingold, G.: Modeling Mesoscale Cellular Structures and Drizzle in Marine Stratocumulus. Part I: Impact of Drizzle on the Formation and Evolution of Open Cells, J. Atmos. Sci., 66, 3237–3256, https://doi.org/10.1175/2009JAS3022.1, 2009a.

20 Wang, H. and Feingold, G.: Modeling Mesoscale Cellular Structures and Drizzle in Marine Stratocumulus. Part II: The Microphysics and Dynamics of the Boundary Region between Open and Closed Cells, J. Atmos. Sci., 66, 3257–3275, https://doi.org/10.1175/2009JAS3120.1, 2009b.

Wood, R. and Bretherton, C. S.: On the Relationship between Stratiform Low Cloud Cover and Lower-Tropospheric Stability, J. Climate, 19, 6425–6432, https://doi.org/10.1175/JCLI3988.1, 2006.

25 Xue, H. and Feingold, G.: Large-Eddy Simulations of Trade Wind Cumuli: Investigation of Aerosol Indirect Effects, J. Atmos. Sci., 63, 1605–1622, https://doi.org/10.1175/JAS3706.1, 2006.

Supplementary information

S1 Track identification with N_d and near IR
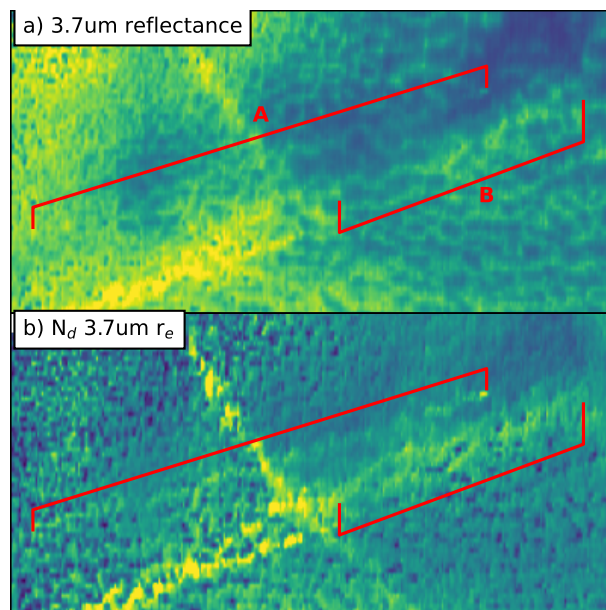
Figure S1. A section from the MODIS Aqua 2015.001.2210 Granule, showing shiptracks in the Californian deck. a) The 3.7 μm reflectance, b) the adiabatic N_d calculated using the 3.7 μm r_e. The colourscales have been adjusted to give roughly equal contrast across the image.

Not all shiptracks are easily visible in the near-IR imagery. The example in Fig. S1 shows a case (A), where a shiptrack visible in the N_d field is not visible in near-IR imagery. Similarly, a shiptrack (B) that is initially visible in the near-IR imagery apparently disappears, while remaining visible in the N_d imagery.